RESEARCH ARTICLE

CRYSTAL Research&Technology

www.crt-journal.org

An Investigation on Structure, AC Conductivity, and Dielectric Characteristics of $Ni_{0.6}Cu_{0.2}Zn_{0.2}Pd_{3x}Fe_{2-2x}O_4$ ($x \leq 0.1$) Nanospinel Ferrites

M.A. Almessiere, A. Baykal, Sagar E. Shirsath, A.V. Trukhanov, A. Demir Korkmaz, and A. Mihmanli*

Partially palladium (Pd) substituted $Ni_{0.6}Cu_{0.2}Zn_{0.2}Pd_{3x}Fe_{2-2x}O_4$ ($x \leq 0.1$) nano-spinel ferrites ($NCZPd_x$ ($x \leq 0.1$) NSFs) have been manufactured via sol–gel combustion route. The phase of all samples has been endorsed by XRD diffraction analysis. Their crystallite size (D_{XRD}) were estimated within 36–72 nm range. Morphology and the chemical composition have been confirmed by EDX (Energy Dispersive X-ray) and SEM-TEM (Scanning-Transmission Emission Microscopy) respectively. Complex impedance spectroscopy (CIS) was utilized to explore the dielectric characteristics within 20 to 120 °C temperature and from 1 to 106 Hz frequency ranges. The two-dimentional frequency and temperature dependencies of the real and imaginary components of permittivity ($\epsilon^{/}$ and $\epsilon^{//}$), the dielectric loss tangent (tan(δ)), the real and imaginary parts of dielectric modulus ($M^{/}$ real and $M^{//}$), σ ac-conductivity (s), the real and imaginary components of impedance ($Z^{/}$ and $Z^{//}$), along with the experimental Nyquist diagrams $Z^{//}(Z^{/})$, were constructed and illustrated for all samples. The main feature of the frequencybehavior of the tan(δ) dielectric loss tangent is the presence of pronounced maxima depending on both frequency and temperature. The maximum value of the tan(δ) observed for the significantly doped x = 0.06-0.10 samples. The Pd substitution changes the electron relaxation and microwave absorption resonance.

1. Introduction

As an important member of the spinel ferrite (SFs) family, NiCuZn NSFs have superior magnetic and electromagnetic characteristics at lower sintering temperatures and high-frequencies compared to other SFs, high electrical resistivity, low dielectric losses, appreciable permeability at intermediate to high frequencies, exceptional chemical stability, etc. Hence, they are currently used in storage applications, cancer treatment, transformers, data storage systems, photo-catalysts, medical applications, magnetic nano-fluids, as sensors, as microwave absorbers, computer circuitry, as multi-layer chip inductors and capacitors (MLCI and MLCC), etc.[1–8]

To improve various performances of NiCuZn NSFs, foreign metal ions (transition metals or rare earth elements) are substituted to the position of Fe^{3+} ion. Almessiere et al.[9] adopted the sonochemical route to enhance the electrical-dielectric characteristics of

M. Almessiere
Department of Biophysics
Institute for Research and Medical Consultations (IRMC), Imam Abdulrahman Bin Faisal University
P.O. Box 1982, Dammam 31441, Saudi Arabia
E-mail: malmessiere@iau.edu.sa

M. Almessiere
Department of Physics
College of Science
Imam Abdulrahman Bin Faisal University
P.O. Box 1982, Dammam 31441, Saudi Arabia

A. Baykal
Department of Food Engineering
Faculty of Engineering, Istanbul Aydin University
Istanbul 34295, Türkiye

A. Baykal
Basic Pharmacy Department
Pharmacy Faculty
Istanbul Aydin University
Istanbul 34295, Türkiye

S. E. Shirsath
School of Materials Science and Engineering
The University of New South Wales
Sydney, NSW 2052, Australia

A. Trukhanov
Smart Sensors Laboratory, Department of Electronic Materials Technology
National University of Science and Technology MISiS
Moscow 119049, Russia

A. D. Korkmaz
Department of Chemistry
Istanbul Medeniyet University
Uskudar, Istanbul 34700, Turkey

A. Mihmanli
Faculty of Dentistry
Gelişim University
Avcılar, Istanbul 34310, Türkiye

A. Trukhanov
2- State Scientific and Practical Center for Materials Science of the National Academy of Sciences of Belarus
Minsk 220072, Belarus

DOI: 10.1002/crat.202500008

Cu-Ni-Zn NSFs by La^{3+} and Y^{3+} ions substitution. Unal et al.[10] studied the electric-dielectric traits of Gd^{3+}-Ga^{3+} ions co-substituted NiZnCu NSFs. Suresh et al.[1] explored the structural, magnetic characteristics and DC electrical resistivity of Sm^{3+} substituted CuNiZn NSFs. Munir et al.[11] examined the dielectric and magnetic traits of NiCuZn SFs. The magnetic-dielectric characteristics of Mn^{2+} and Nb^{5+}-codoped NiZnCu ferrites were investigated by Cheng et al.[12] In another study, the magnetic and structural traits of Se-substituted CuNiZn NSFs were explored by Baykal et al.[13] Yang et al.[14] explored the electrical and magnetic traits of Cd^{2+} substituted CuNiZn ferrites. The structural and electrical/dielectric properties of Sn^{4+} ion-doped ZnNiCu NSFs were explored by Unal et al.[2] Roy and Bera study demonstrated an enhancement of the electromagnetic properties of CuNiZn NSFs due to Mg^{2+} doping. Korkmaz[15] searched for the effect of Dy^{3+} substituted NiZnCu on various cancer cell lines. Roy et al.[16] investigated the effect of Mg substitution on electromagnetic properties of $(Ni_{0.25}Cu_{0.20}Zn_{0.55})Fe_2O_4$ ferrite.

The present study advances the field of spinel ferrites of Ni, Cu, and Zn by introducing palladium (Pd), a noble metal that is corrosion-resistant. At room temperature, the metal has the unusual property of absorbing up to 900 times its own volume of hydrogen, a fact that makes it an extremely popular catalyst for a wide variety of chemical reactions.[17,18] The combination of transition metal oxide with noble metal is an effective method to improve the performance of H_2-SCR (selective catalytic reduction) catalysts.[19] Palladium is widely employed as a catalytic agent in countless chemical reactions due to its exceptional capability of absorbing 900 times its volume of H_2(g). Xu et al. synthesized the spinel ferrites substituted with Pd to reduce NO with H_2 catalytically at low temperatures as a prominent catalyst.[19] Vlazan et al. examined the magnetic characteristics of Pd-substituted $CoFe_2O_4$.[18]

Therefore, in this study, we report the synthesis of Pd substituted $Ni_{0.6}Cu_{0.2}Zn_{0.2}Pd_{3x}Fe_{2-2x}O_4$ ($x \leq 0.1$) nano-spinel ferrites by sol–gel composition route. The crystallographic features of nanoparticles were explored by X-ray crystallography. The Pd^{2+} ion substitution on the structure and electric/dielectric $Ni_{0.6}Cu_{0.2}Zn_{0.2}Pd_{3x}Fe_{2-2x}O_4$ ($x \leq 0.1$) nano-spinel ferrites have been investigated in detail.

2. Results and Discussion

2.1. Structure and Morphology

The X-ray powder diffraction pattern of the nanocomposites consisting of NCZ**Pd**$_x$ ($x \leq 0.1$) NSFs is depicted in **Figure 1**. The entirety of the samples exclusively exhibits singular peaks of cubic spinel ferrite; none of the samples include any other phases either. Through this observation, it became apparent that the Pd ions had successfully integrated themselves into the crystallographic sites of the $Ni_{0.6}Cu_{0.2}Zn_{0.2}Fe_2O_4$ NSFs, resulting in the formation of a clearly defined cubic spinel. The Rietveld refinement of the XRD pattern was applied via Match 4! and full-proof software for calculating the structural parameters as listed in **Table 1**. Due to the distortion that occurred in the cubic crystal, the lattice parameter "a_o" was obtained, and it displayed a variation with substitution by Pd. Scherrer's formula was applied to

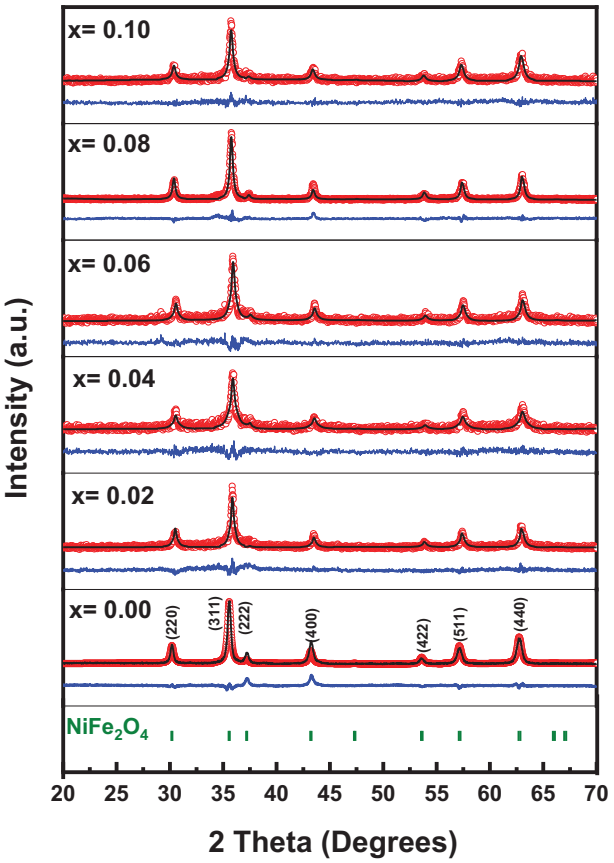

Figure 1. X-ray powder pattern of NCZ**Pd**$_x$ ($x \leq 0.1$) NSFs.

the (311) peak in order to determine the average crystallite size, which was found to be between 36 and 72 nm.[22] The influence of Pd substitution was also observed in the crystallite size (D_{XRD}), which was computed. In **Figure 2**, the morphology of NCZ**Pd**$_x$ ($x \leq 0.1$) NSFs is exhibited. Images revealed a significant cubic particle that was clumped together.

The EDX spectrum characterization of NCZ**Pd**$_x$ ($x = 0.04$ and 0.10) NSFs is depicted in **Figure 3**. The values of x are 0.04 and 0.10. The EDX peaks are a representation of the elemental content that is expected to be present in the NPs that are created. The product that was created was discovered to contain elements such as Ni, Cu, Zn, Pd, Fe, and O. The TEM and HR-TEM images of NCZ**Pd**$_x$ ($x = 0.04$) NSFs were displayed in **Figure 4**. The TEM images revealed the spherical shape. The particle size distribution was estimated by imageJ software and found in a range of 50 nm. The HR-TEM analysis was employed to identify a pure spinel ferrite structure. The distance between lattice fringes was measured using Gatan software, and the results were consistent with the XRD findings. The distances were 0.14, 0.16, and 0.24 nm, which correspond to the (440), (333), and (222) planes of the cubic spinel structure of ferrites.

$$L(A) = a \cdot \sqrt{3/4}) \quad (1)$$

$$L(B) = a \cdot \sqrt{2/4}) \quad (2)$$

Table 1. Refined structural parameters of NCZ**Pd**$_x$ ($x \leq 0.1$) NSFs (structural parameters (a_o), crystal size (D_{xrd}), cell volume (V), X-ray density (d_x), Chi-square (χ^2), Bragg R factor (R_{Bragg}), hopping lengths L(A) and L(B), specific surface area (S_{Ar}), and Polaron radius (γ_p).

X	a [Å]	d_x [g cm^{-3}]	V [Å]^3	D_{XRD} [nm] ±0.03	χ^2	R_{Bragg}	L(A)	L(B)	S_{Ar} [g m^{-2}]	γp
0.00	**8.3786**	5.209	588.1856	43.6	5.2	15.0	3.628	2.962	26.419	0.737
0.02	**8.3752**	5.441	587.4741	72.5	1.3	19.8	3.627	2.961	15.210	0.737
0.04	**8.3737**	5.454	587.1459	36.2	1.0	26.2	3.626	2.961	30.390	0.737
0.06	**8.3791**	5.444	588.2993	43.5	1.0	26.0	3.628	2.962	25.336	0.737
0.08	**8.3665**	5.495	585.6431	51.3	1.2	10.5	3.623	2.958	21.285	0.736
0.10	**8.3700**	5.225	586.3700	54.4	0.8	17.1	3.624	2.959	21.109	0.737

The tetrahedral and octahedral hopping lengths (L(A) and L(B), consequently), can be determined by:

γ_p is known as the Polaron radius

$$\gamma_p = \frac{1}{2} \times \left(\sqrt[3]{\frac{\pi \times a^3}{576}} \right) \quad (3)$$

Hopping lengths L(A) and L(B) denote the distance for hopping in magnetic ions in sublattice sites A and B, respectively (**Figure 5**). In addition, they are indicators of charge carriers shifting from a cationic site to the other cationic site.[23] An increasing hopping length means more potential is necessary to move a charge carrier. A decrease in Polaron radius means less energy is required to transfer charge carriers and *vice versa*.[24] Except for x = 0.08, there is a general decreasing trend as the concentration of Pd^{2+} rises in NCZPd$_x$ ($x \leq 0.1$) NSFs for both hopping length and Polaron radius.[25,26] This might be related to the drop in the lattice parameter.[27] In addition, L(A) being larger than L(B) shows that the possibility of an electron hopping from A to B is less than its possibility of moving between B and B sites.[28]

The specific surface area (S_{Ar}) of the nanoparticles in g m^{-2} can be expressed by the following equation:

$$S_{Ar} = 6000 / \left(d_x \cdot D_{XRD} \right) \quad (4)$$

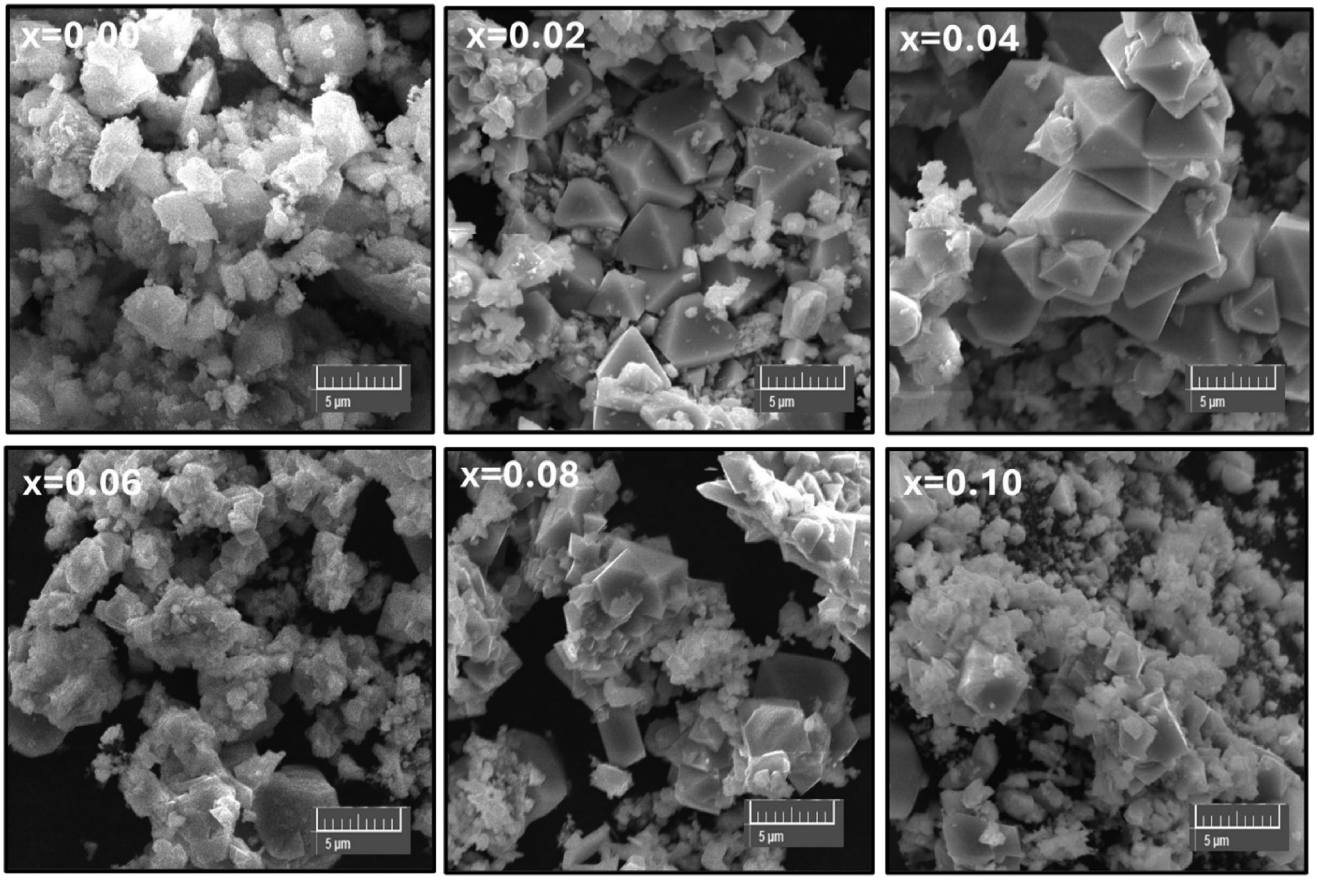

Figure 2. SEM micrographs of NCZ**Pd**$_x$ ($x \leq 0.1$) NSFs.

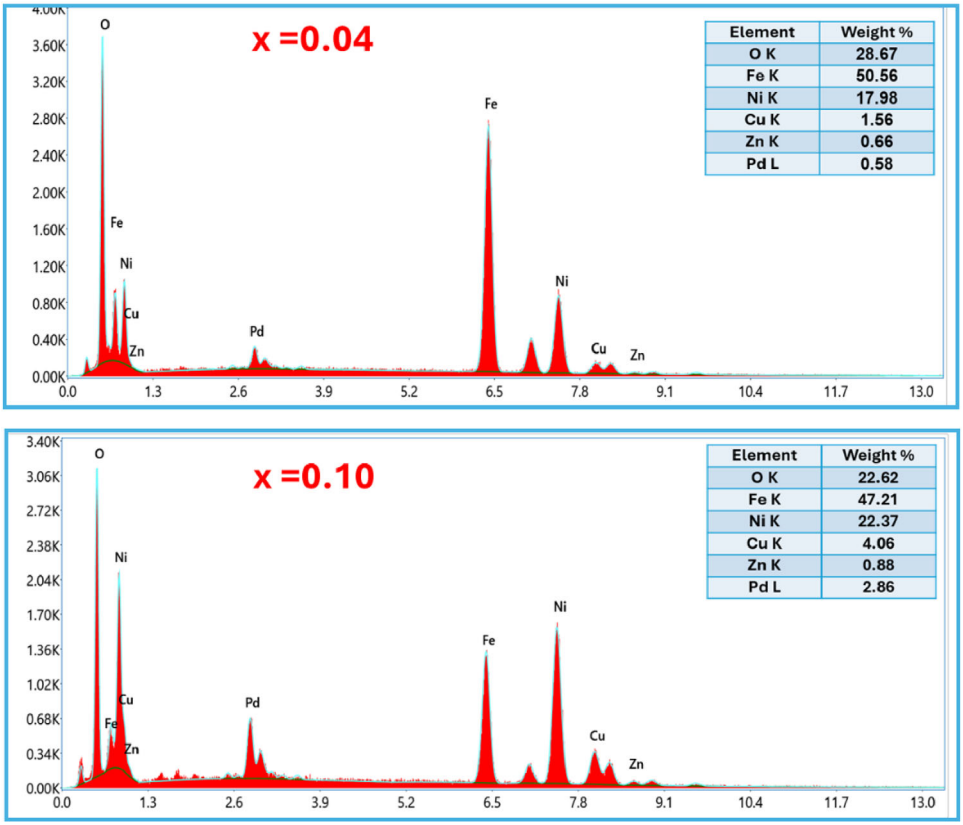

Figure 3. EDX spectrum of NCZ**Pd**$_x$ (x = 0.04 and 0.10) NSFs.

In which 6000 is known as the form factor for spherical structures. The sol–gel autocombustion technique is notorious for the synthesis of high-surface area materials.[29] The specific surface area of products ranges between 15.210 and 30.390 g m^{-2}. A large surface area is needed for supercapacitor and gas sensing applications. Therefore, x = 0.04 can be a good candidate to apply NCZPd$_x$ (x ≤ 0.1) NSFs for such uses.[29,30]

2.2. Dielectric Properties

To investigate the effect of the substitution of Fe^{3+} ions by Pd^{3+} ions on the dielectric properties of $Ni_{0.6}Cu_{0.2}Zn_{0.2}Fe_2O_4$ (x ≤ 0.1) NSFs, the CIS (complex impedance spectroscopy) was used in the frequency of 1–10^6 Hz and temperature of between 20–120 °C.

Figure 6 shows the frequency dependence of the ϵ' permittivity real part at different temperatures from 20 up to 120 °C for all the samples studied. It is clearly seen that the ϵ' permittivity real part gradually decreases slowly with increasing frequency as it is usually observed for magnetically hard ferrite spinels.[31] The curves at different temperatures actually merge above 1 kHz, while the low-frequency part increases significantly with increasing temperature. It is clearly seen that these presented curves are monotonically increasing depending on the temperature. This feature is clearly fixed in the region of small and medium frequencies. It can be concluded that the ϵ' permittivity real part follows an exponential law depending on the frequency.[32]

This behavior of the ϵ' permittivity real part is explained by the phenomenon of electron relaxation, which is typical for deep dielectrics with a high degree of charge localization.[33] Localized charges create stable dipoles, while the overall polarization of the system diminishes as frequency increases. A strong correlation is observed between the ϵ' permittivity real part and the total polarization of the system.[34] At low frequencies, the dipoles exhibit sensitivity to alterations in the orientation of the applied field; conversely, as frequency increases, the dipoles of the examined medium exhibit a lag in their response to changes in the external field's direction.[35] It should be noted that weak doping doses of 0.02–0.04 lead to an explosive growth of the ϵ' permittivity real part. This behavior is explained by the introduction of chemical defects[36] in the crystal lattice and a high degree of disorder in their spatial arrangement.[37]

In addition, it is necessary to consider that the samples are ceramic, and to explain the dielectric properties it is necessary to consider the so-called core–shell model,[38] according to which the crystallites consist of a highly conductive core and a low-conductive shell. The bound charges, the mass fraction of which is higher in the shell, which is the surface layer of the crystallite, determine the polarization of the sample. Since the dimensions of the shell are smaller than the dimensions of the core, the contribution of the surface layer of the crystallite is dominant at low frequencies.

The frequency dependence of the ϵ'' permittivity imaginary part is shown in **Figure 7**. The main trends in its behavior largely correlate with the change in its real part. The ϵ'' permittivity

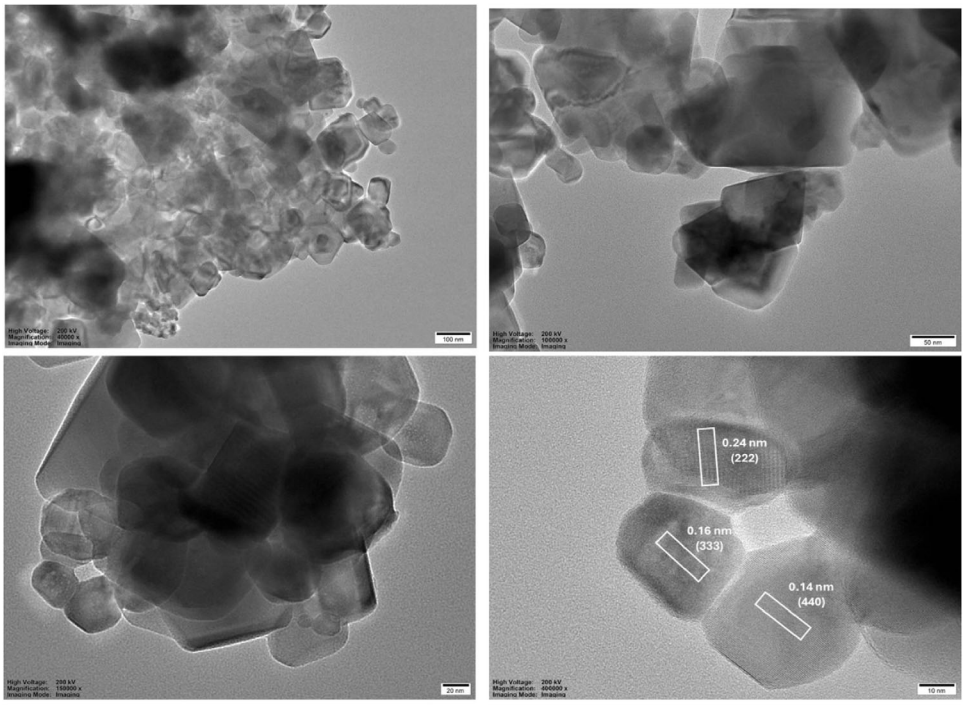

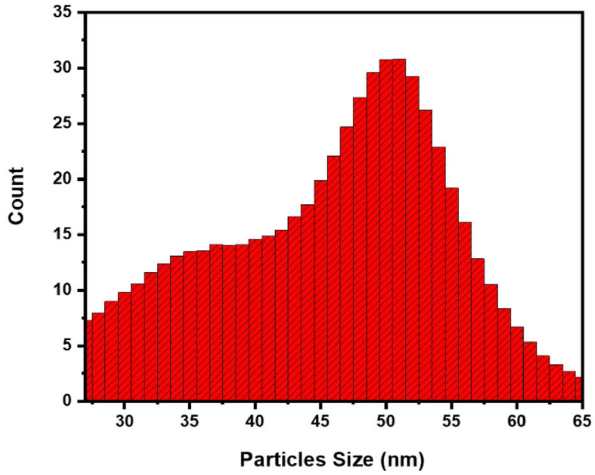

Figure 4. TEM, HR-TEM images, and particle size distribution histogram of $NCZPd_x$ (x = 0.04) NSFs.

imaginary part characterizes the absorption processes of the system, in which the maxima of this function are observed in the vicinity of certain resonance frequencies.

Microwave losses in condensed matter are determined mainly by the scattering of both itinerant and localized light electron charges.[39] The scattering of itinerant charges in ferrites is almost absent, while the electrical conductivity of partially localized charges is due to hopping conductivity.[40] The scattering of completely localized charges is described by spatial and surface polarization, as well as dipole relaxation.[41] The scattering intensity of partially localized charges is determined by such unit cell parameters as the average covalent bond length and average covalent bond angle,[42] as well as the average valence of cations in tetrahedral and octahedral positions.[43] The scattering intensity of completely localized charges is also determined by the structural parameters and the average valence of cations. In addition, the scattering intensity depends on the homogeneity of the condensed medium and the distortions of the near-surface layer.

The substitution of $\mathbf{Fe^{3+}}$ ions by $\mathbf{Pd^{2+}}$ **ions** affects these mechanisms and changes the dielectric losses of the considered ferrite-spinels. Namely, such a substitution changes the average valence and concentration of iron cations and, consequently, changes the hopping conductivity of partially localized charges between Fe^{2+} and Fe^{3+} cations. The introduction of Pd^{2+} cations into the crystal lattice of ferrite-spinels changes the hopping frequency, thereby changing the dielectric losses. In addition, Pd^{2+} cations change the average crystallite size, which affects the ratio of the polarizations of the bulk and surface fully localized charge in the near-surface layer of crystallites and also changes the dielectric losses. In addition, low substitution levels tend to reduce the dielectric

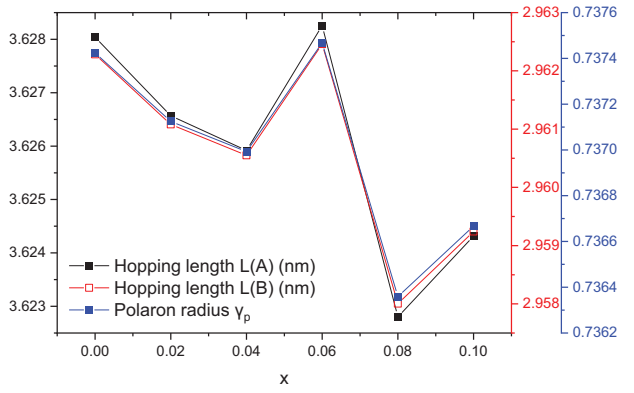

Figure 5. Hopping length (LA and LB) and Polaron radius versus concentration x in $NCZPd_x$ ($x \leq 0.1$) NSFs.

losses due to the improved connectivity of the near-surface layers of crystallites within the grains.

It should be noted that a pronounced maximum is observed only for the undoped x = 0.00 sample at low frequencies. This maximum shifts to the high-frequency region with increasing temperature. For this sample, a tendency toward a maximum in the high-frequency region is also observed, which is independent of temperature. For some doped samples x = 0.2-0.10, a weakly expressed maximum is observed at moderate frequencies.

Figure 8 shows the frequency dependence of the tan(δ) dielectric loss tangent. The curves presented mainly correlate with the behavior of $\epsilon^{//}$. A characteristic feature of the frequency behavior of the tan(δ) dielectric loss tangent is the presence of pronounced maxima depending on both frequency and temperature.

Increasing temperature leads to an increase in the mobility of partially localized charges. This behavior increases losses due to the intensification of processes of volume and surface polarization and dipole relaxation. Phase and structural transitions can change the scattering intensity with increasing temperature. However, such facts were not recorded when substituting Pd^{2+} cations. The substitution concentration has a significant effect on the change in scattering intensity. At low substitution concentrations, the scattering intensity shows increased efficiency due to an increase in polarization and a decrease in partial localized charge. This results in more efficient energy storage and lower losses. As the substitution concentration increases, the scattering intensity changes depending on the distribution of the substituent cations between the lattice sites. Substitution increases polarization and also introduces lattice defects and/or distortions that affect energy scattering. The scattering intensity increases due to large lattice distortions and defects that contribute to energy losses. The scattering intensity generally decreases with increasing frequency. It is an important parameter indicating the energy loss in a material due to dielectric relaxation and conductivity losses.

It should also be noted that the maximum value of the tan(δ) (dielectric loss tangent) observed for samples significantly doped x = 0.06–0.10. This behavior of the tan(δ) dielectric loss tangent is explained by the Maxwell–Wagner model, which assumes that the dielectric medium is formed by grains consisting of a conducting core and an insulating near-surface layer.[44] At low frequencies, the charge concentration in the near-surface layer is high. This leads to high absorption values and an increase in tan(δ). At high frequencies, charges accumulate mainly inside the core, leading to a decrease in tan(δ).

The frequency dependence of the real $M^{/}$ and imaginary $M^{//}$ parts of the dielectric modulus are shown in **Figures 9** and **10**. It is clearly seen that the $M^{/}$ dielectric modulus real part mainly increases with increasing frequency and temperature.

The complex modulus of dielectric compounds and composites is a suitable tool used to analyze relaxation phenomena and viscoelastic processes.[45] This value gives a detailed idea of the molecular dynamics, phase transitions, and other intrinsic properties of the studied materials.[46] The complex modulus is mainly used to study dielectric relaxation in materials in which the charge motion is determined by the orientational polarizability of permanent dipoles. In this case, the position of the frequency peak in the imaginary part of the permittivity determines the characteristic time boundary of the orientational ionic and/or molecular mobility. In the case of ion-conducting glasses and/or melts, the imaginary part of the permittivity incorrectly sets the time boundary for ionic and/or molecular mobility. Therefore, knowledge of the dielectric modulus $M^*(f) = 1/\epsilon^*(f)$ gives more accurate information about the nature of relaxation, where the effects of simple DC conductivity appear as a pronounced peak similar to the Debye peak in Ref. [47]. The frequency of the complex modulus peak is well recognized as delineating the spectrum into two distinct sections. To the left of the peak, partially localized charges exhibit mobility over extensive distances, whereas, to the right of the peak, partially localized charges are spatially restricted within potential wells and can only traverse limited distances.[48] A shift in the peak frequency toward higher values with a change in substitution concentration and temperature indicates a thermally activated process.[49]

The resonance frequency of the absorption peaks for the $M^{//}$ dielectric modulus imaginary part increases with increasing temperature, which indicates a thermally activated process. The area to the left of the maximum is understood to represent processes within the grain core, characterized by highly mobile charges over extensive distances, whereas the area to the right of the maximum pertains to processes in the grain near-surface layer, where charge carriers are confined in potential wells and can only traverse short distances. Assuming that the imaginary component of the M″ dielectric modulus demonstrates thermally activated relaxation processes, one can compute the activation energy (Ea) necessary for charge transfer and conductivity.[50]

Knowledge of conductivity on alternating current (σ) is necessary for studying the characteristics of charge carriers and the mechanism of conductivity of condensed matter. For ferrites, the carriers are partially localized electrons and holes,[51] which participate in hopping charge transfer with variable length known as variable range hopping (VRH)[52] described by the Mott[53] or Efros–Shkovskii[54] models with competitive interaction.[55]

Knowledge of the frequency behavior of ac-conductivity is also important for understanding the dielectric properties of the medium since this reveals the nature of the movement of charge carriers, and many dielectric parameters depend on this. Frequency dependence of the σ ac-conductivity is presented in **Figure 11** for all the samples studied.

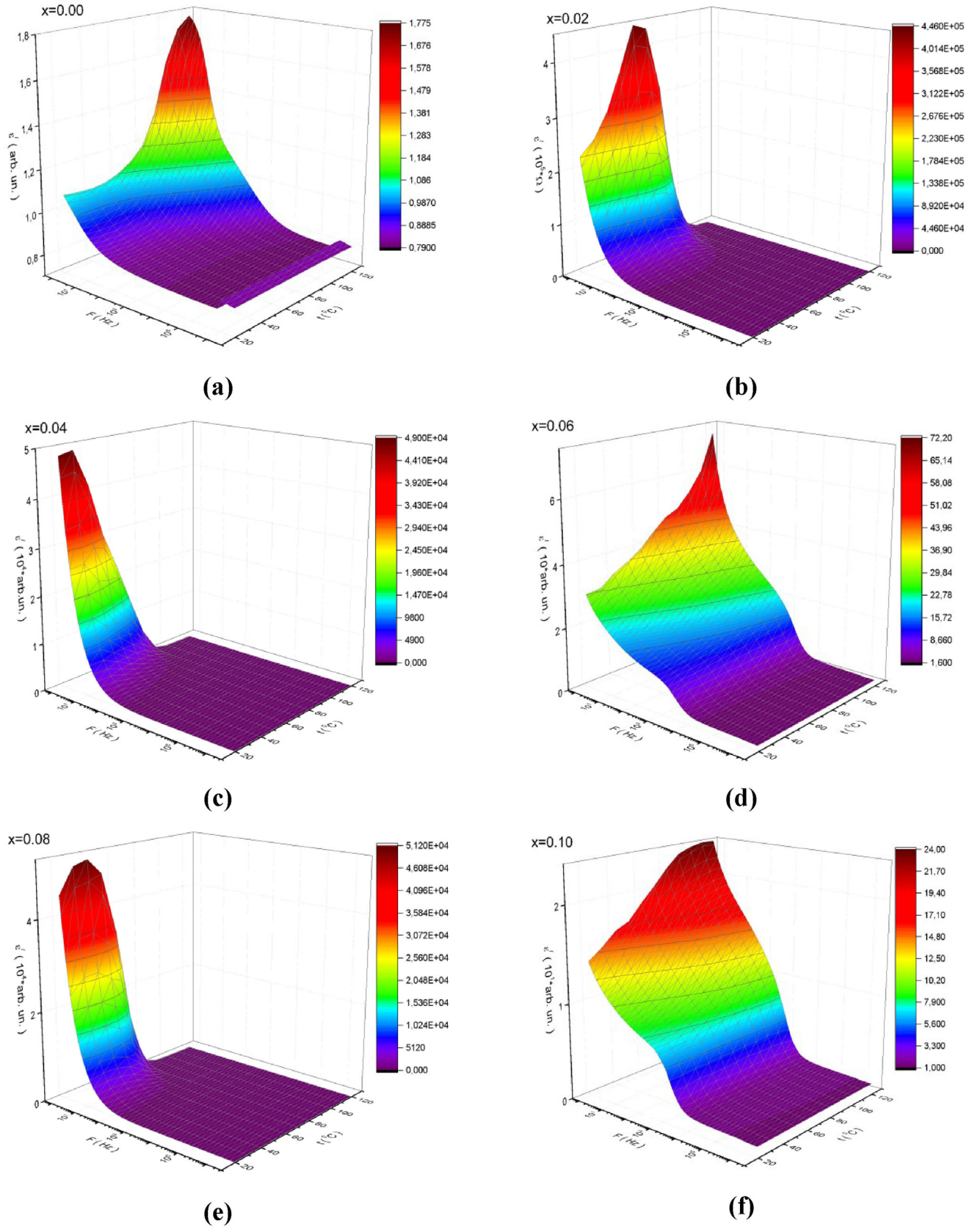

Figure 6. a–f). Frequency dependence of ϵ' permittivity real part at different Ts of NCZPd_x ($x \leq 0.1$) NSFs.

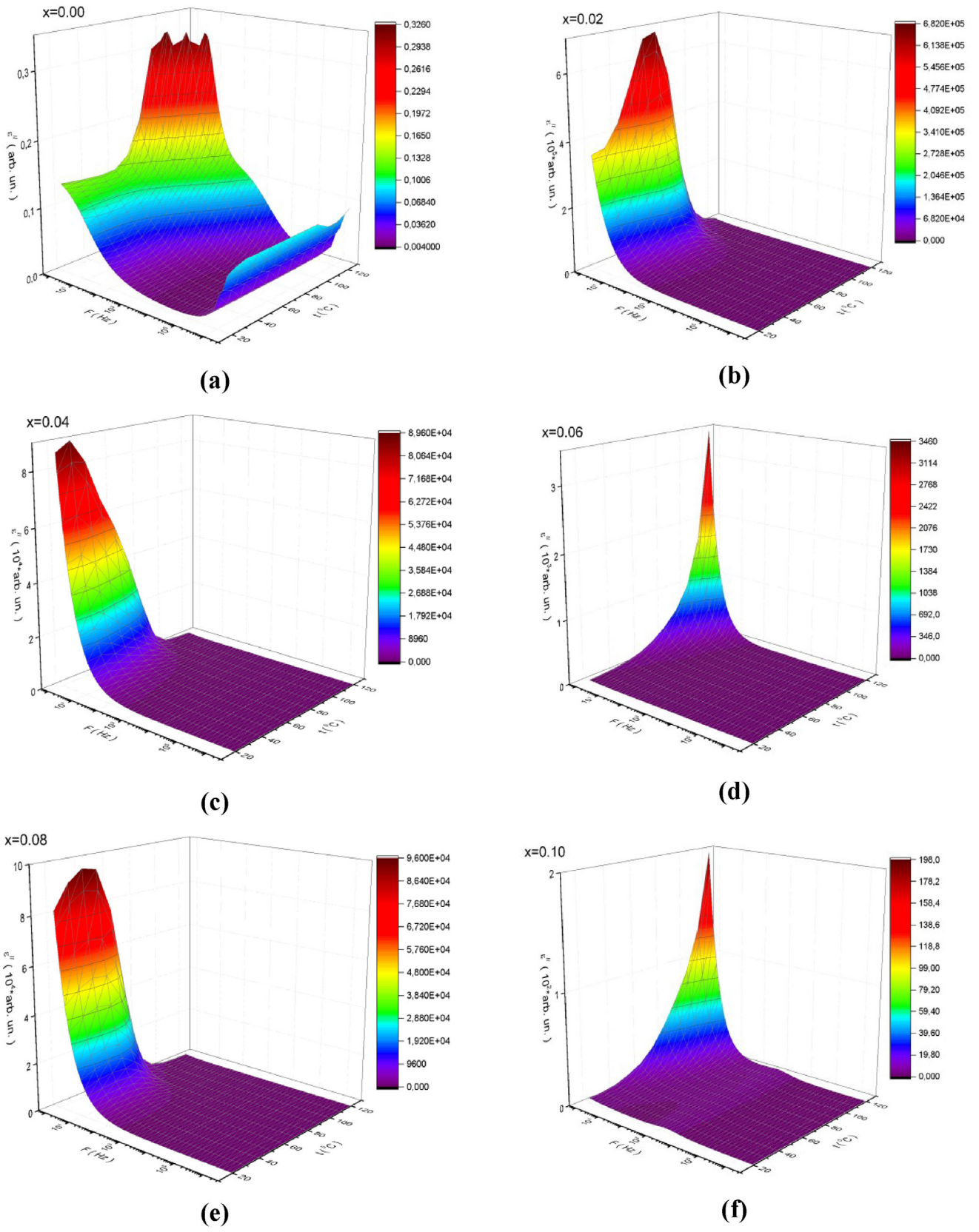

Figure 7. a–f). Frequency dependence of $\epsilon^{//}$ permittivity imaginary part of NCZ**Pd$_x$** ($x \leq 0.1$) NSFs.

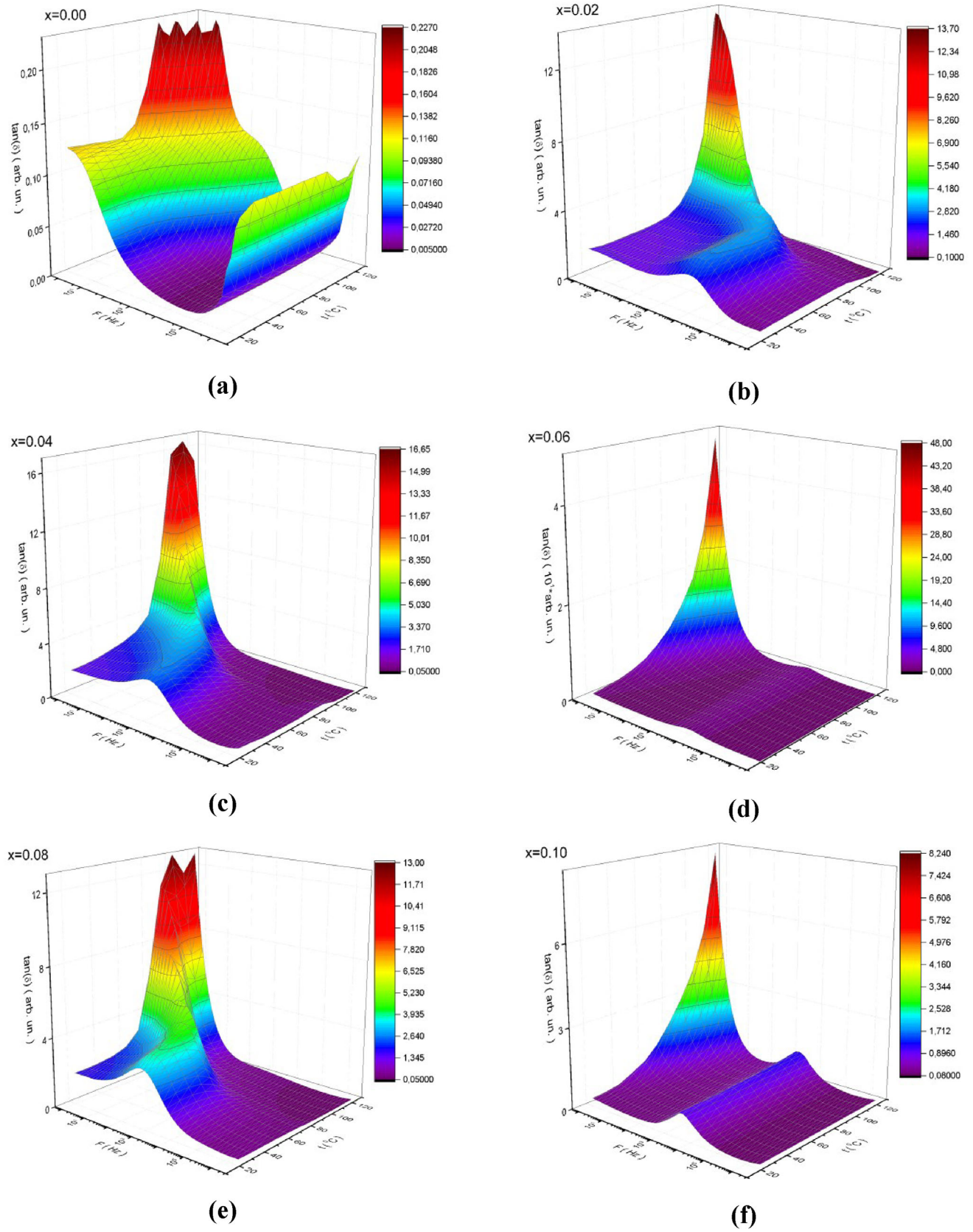

Figure 8. a–f). Frequency dependence of tan(δ) (dielectric loss tangent) of NCZ**Pd**$_x$ ($x \leq 0.1$) NSFs at different temperatures.

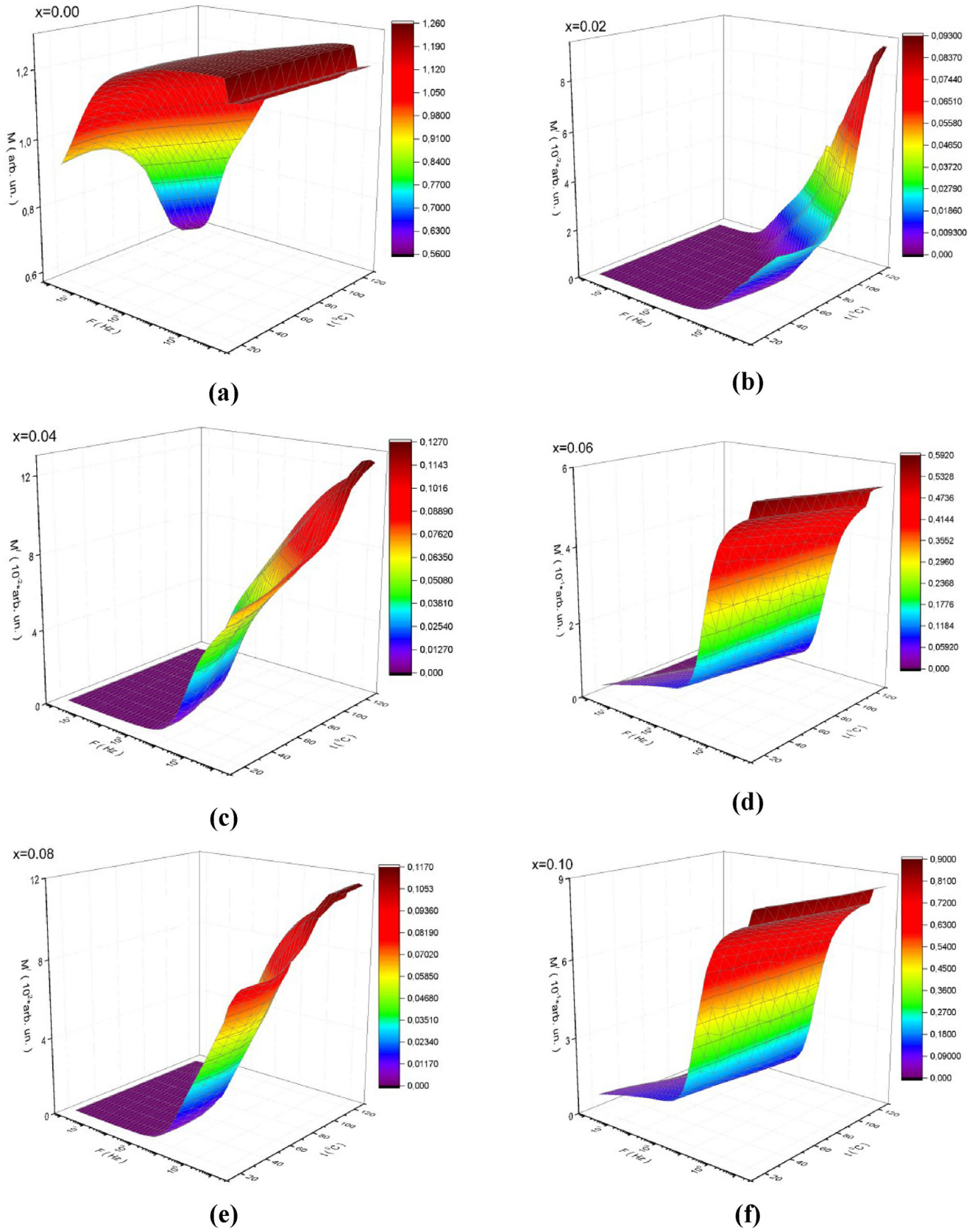

Figure 9. a–f). Frequency dependence of M/ dielectric modulus real part of NCZ**Pd**$_x$ ($x \leq 0.1$) NSFs at different Ts.

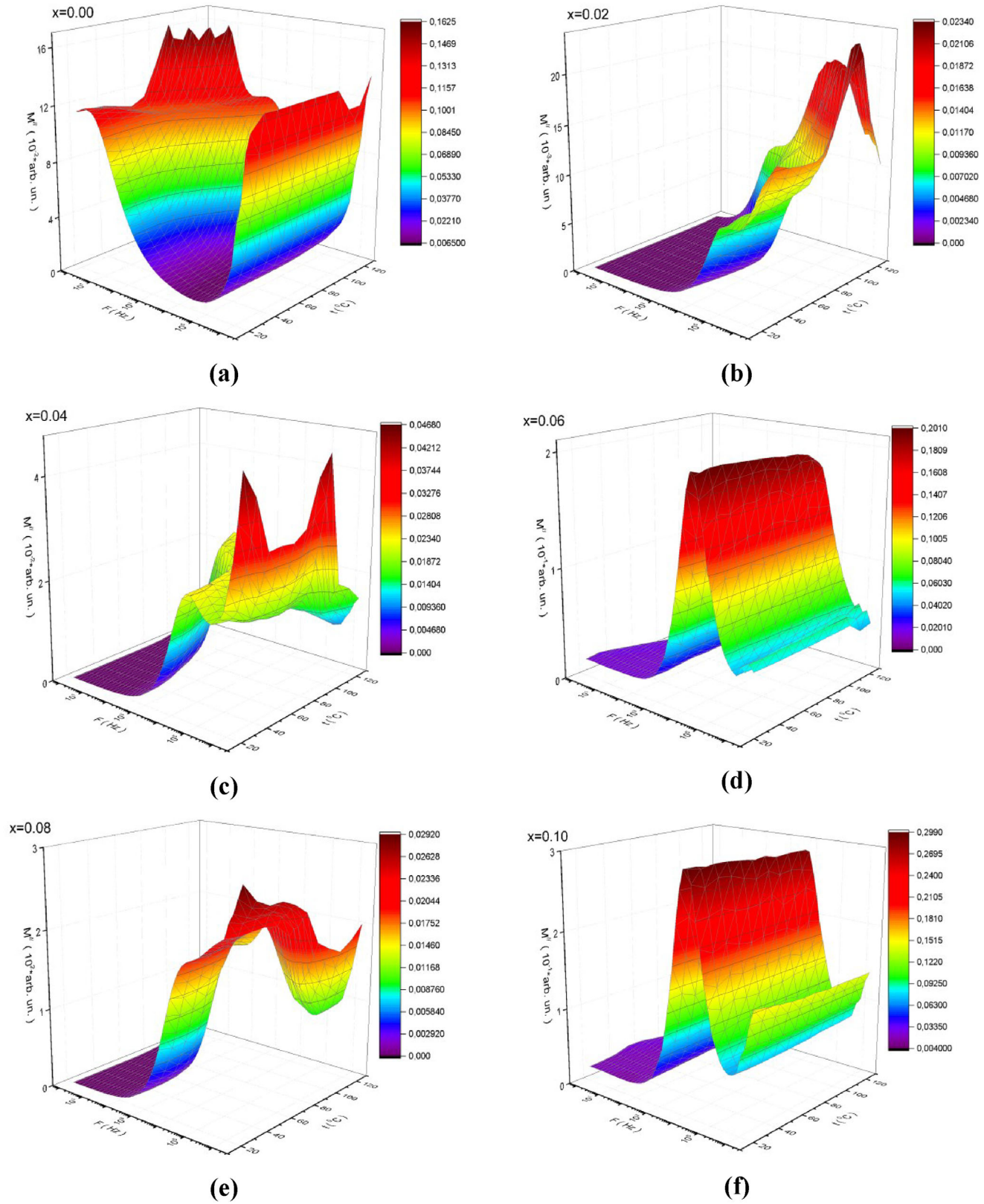

Figure 10. a–f). Frequency dependence of $M^{//}$ dielectric modulus imaginary part of NCZ**Pd**$_x$ ($x \leq 0.1$) NSFs at different temperatures.

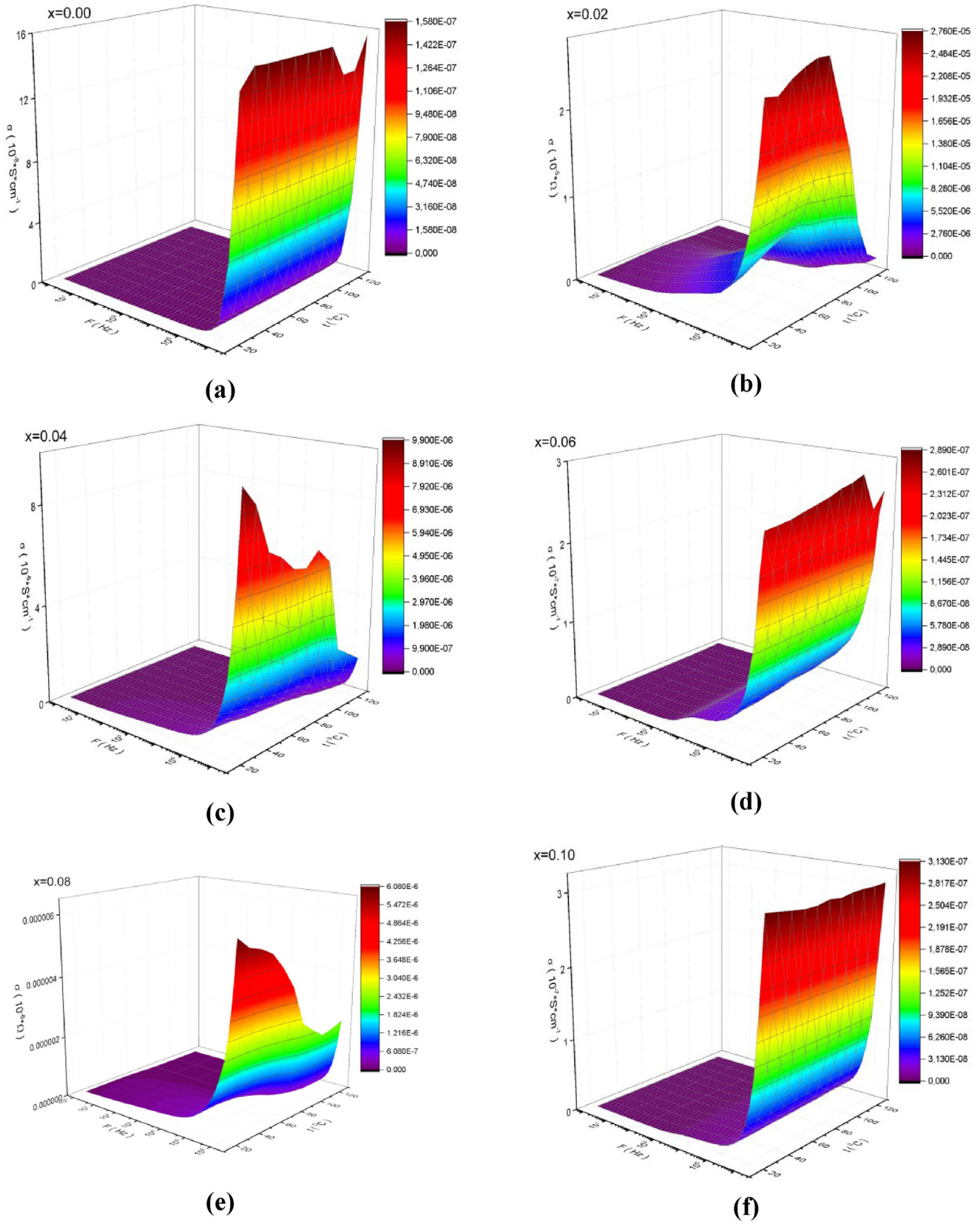

Figure 11. a–f). Frequency dependence of σ ac-conductivity of NCZPd_x ($x \leq 0.1$) NSFs at different temperatures.

The substitution by Pd^{2+} cations noticeably affects the ac-conductivity, changing both the frequency and length of the hopping and the dynamics of polarization. The ac-conductivity of palladium cations substituted also depends on the frequency of electromagnetic radiation and on temperature. At low frequencies, the ac-conductivity tends to increase moderately with increasing substitution concentration. This increase can be explained by an increase in the mobility of charge carriers, while the scattering charge carriers at defects and grain boundaries will also increase. At high frequencies, the conductivity of alternating current tends to increase significantly depending on external conditions.

When analyzing the behavior of this quantity, two regions should be distinguished: low-frequency and high-frequency. The first region is located at low frequencies, where conductivity is determined mainly by the contribution of direct current (DC) and is virtually independent of frequency. The second region is located at high frequencies, where the conductivity is determined primarily by the frequency-dependent conductivity, which increases rapidly with increasing frequency. This sharp increase in conductivity observed at high frequencies is attributed to the contribution of localized charge carriers, which can perform thermally activated jumps and follow Jonscher's power law[56] for nanosized crystallites. This law is expressed as:

$$\sigma(\omega) = \sigma dc + A\omega^{n} \quad (5)$$

where $\sigma(\omega)$ represents the total AC conductivity, σ_{dc} is the DC conductivity component, A is a temperature-dependent constant, ω is the angular frequency, and n ($0 < n < 1$) is the frequency exponent that characterizes the nature of charge transport, has been used to fit the experimental conductivity data. The analysis revealed that at low frequencies, the conductivity exhibits a frequency-independent plateau, indicating a dominant DC conduction mechanism associated with grain boundary effects and Maxwell–Wagner interfacial polarization. The fitted σ_{dc} values increase with temperature, suggesting thermally activated charge transport. At higher frequencies, the conductivity follows a power-law dependence, demonstrating the transition to hopping conduction mechanisms. The frequency exponent n was found to vary with Pd concentration and temperature, indicating modifications in the charge transport dynamics.

Doping ($x = 0.02$–0.08) the initial solid solution significantly increases conductivity, which also increases with increasing temperature.

The impedance real (Z′) and imaginary (Z″) parts as a function of frequency and temperature were analyzed in detail for all the substitution concentrations, and the results are given in **Figures 12** and **13**. It is clearly seen that the value of Z′ is significant at low frequencies. This behavior is explained by the fact that partially localized charge carriers in the near-surface layer of the crystallite, where high resistance is observed, make the main contribution to the conductivity. As the frequency increases, partially localized charge carriers from the depth of the crystallite, where the resistance is lower than the surface resistance, which lead to a decrease in the Z′ impedance real part. With increasing temperature, the real part of the impedance Z′ tends to decrease. This behavior is associated with an increase in the conductivity of alternating current with increasing temperature. There is also a tendency to convergence in the Z′ spectra at high frequencies and temperatures, which can occur both due to the release of space charges and due to a decrease in the energy barrier for separating types of charge carriers.

The Cole–Cole impedance plot or Nyquist diagrams can be employed to clearly distinguish the impedance contributions from the crystallite core and the crystallite surface layer. Such data at different frequency and temperature values for all the substitution concentrations studied are shown in **Figure 14**. The accuracy of the analysis result is contingent upon the selection of an equivalent circuit that is appropriate for representing the dielectric properties. From the microstructural point of view, each sample can be represented by a crystallite core and a crystallite surface layer, which have different AC-conductivity and permittivity.[57] Figure 14 illustrates that the influence of the surface layer on surface charge polarization is pronounced at elevated temperatures. The Cole–Cole plot, characterized by a quasi-semi-circle, is employed to elucidate the relaxation mechanism of different ferrite spinel samples. Considering this aspect enables a better understanding of the sort of dielectric relaxation present in the frequency-dependent response of a specific sample. As temperature rises, the diameter of the quasi-semi-circles in the Cole–Cole plots diminish, indicating a temperature-dependent relaxation mechanism. This type of curve shows that the system is non-Debye. As was mentioned above, it is well known that this type of curve is the result of ionic hopping conductivity between di- and trivalent iron cations with a wide distribution of relaxation times. It may be deduced that at elevated temperatures, an increased number of partially localized charges are thermally excited, thereby reducing the carrier relaxation time. Thermal energy facilitates the alignment of existing dipoles with the oscillations of the external alternating electric field. This mechanism elucidates the presence of temperature-dependent electrical relaxation phenomena in the examined samples.

3. Conclusion

NCZPdx ($x \leq 0.1$) nanospinel ferrites (NSFs) were successfully synthesized via the sol–gel combustion route, and their dielectric and electrical properties were systematically investigated using complex impedance spectroscopy (CIS) over a broad frequency range (1 Hz–10^6 Hz) and temperature range (20–120 °C). The study analyzed the frequency and temperature dependence of key dielectric parameters, including the ϵ' real and ϵ'' imaginary parts of permittivity, tan(δ) dielectric loss tangent, M′ real and M″ imaginary parts of dielectric modulus, σ AC conductivity, Z′ real and Z″ imaginary parts of impedance, and Nyquist diagrams for all compositions. The results showed that the real (ϵ') and imaginary (ϵ'') parts of permittivity gradually decrease with increasing frequency, while their low-frequency values increase significantly with rising temperature, following an exponential law behavior. This dielectric response was attributed to electron relaxation mechanisms and the core–shell model of ceramics, where charge localization and interfacial polarization significantly influence the system's dielectric characteristics. The palladium (Pd^{2+}) substitution played a crucial role in altering electron relaxation processes and microwave absorption resonance, impacting the overall dielectric behavior. A pronounced maximum in ϵ'' was observed in the undoped ($x = 0.00$) sample at low frequencies and temperatures, while the highest dielectric loss tangent (tan δ) was

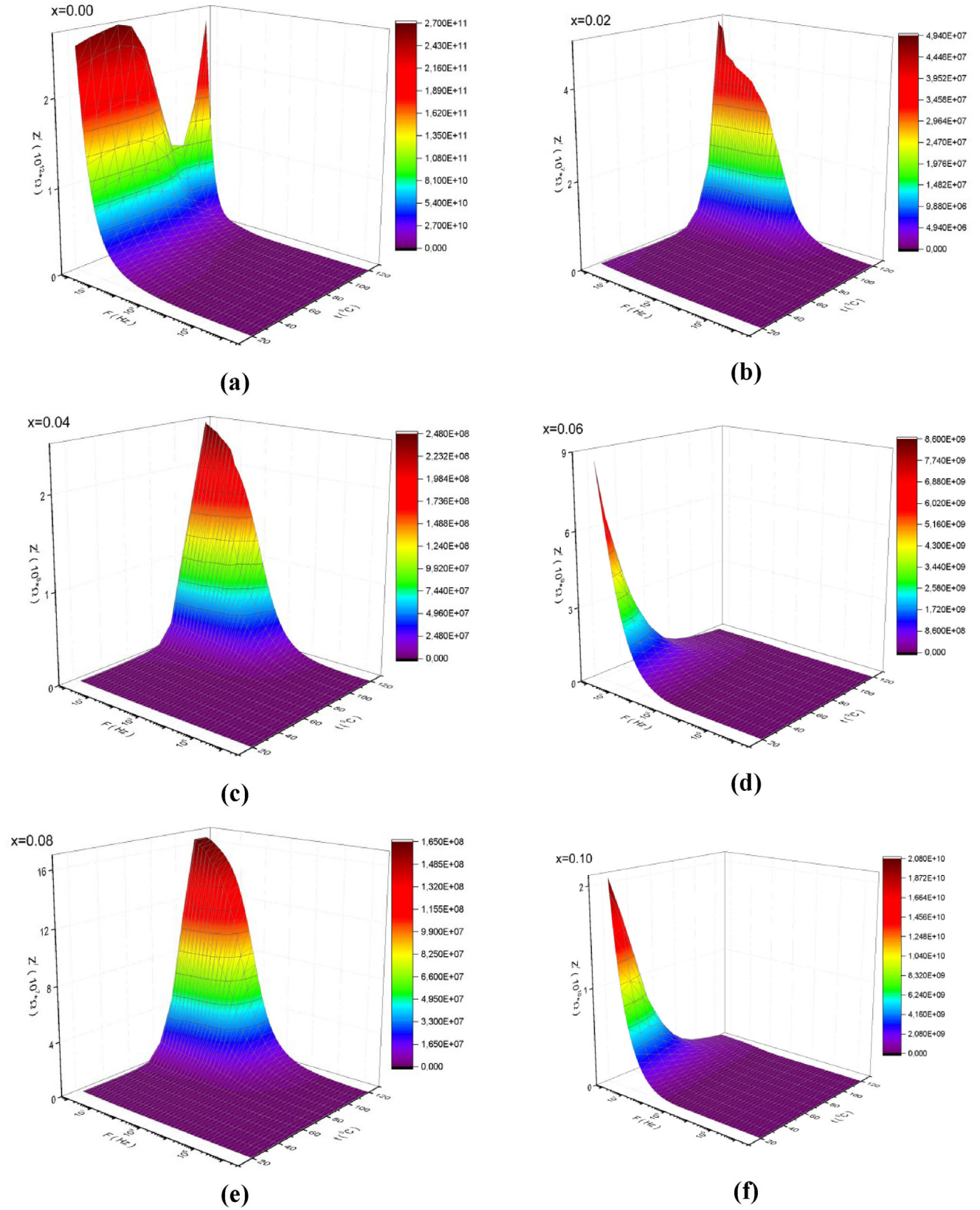

Figure 12. a–f). Frequency dependence of Z/ impedance real part of NCZ**Pd**$_x$ ($x \leq 0.1$) NSFs at different temperatures.

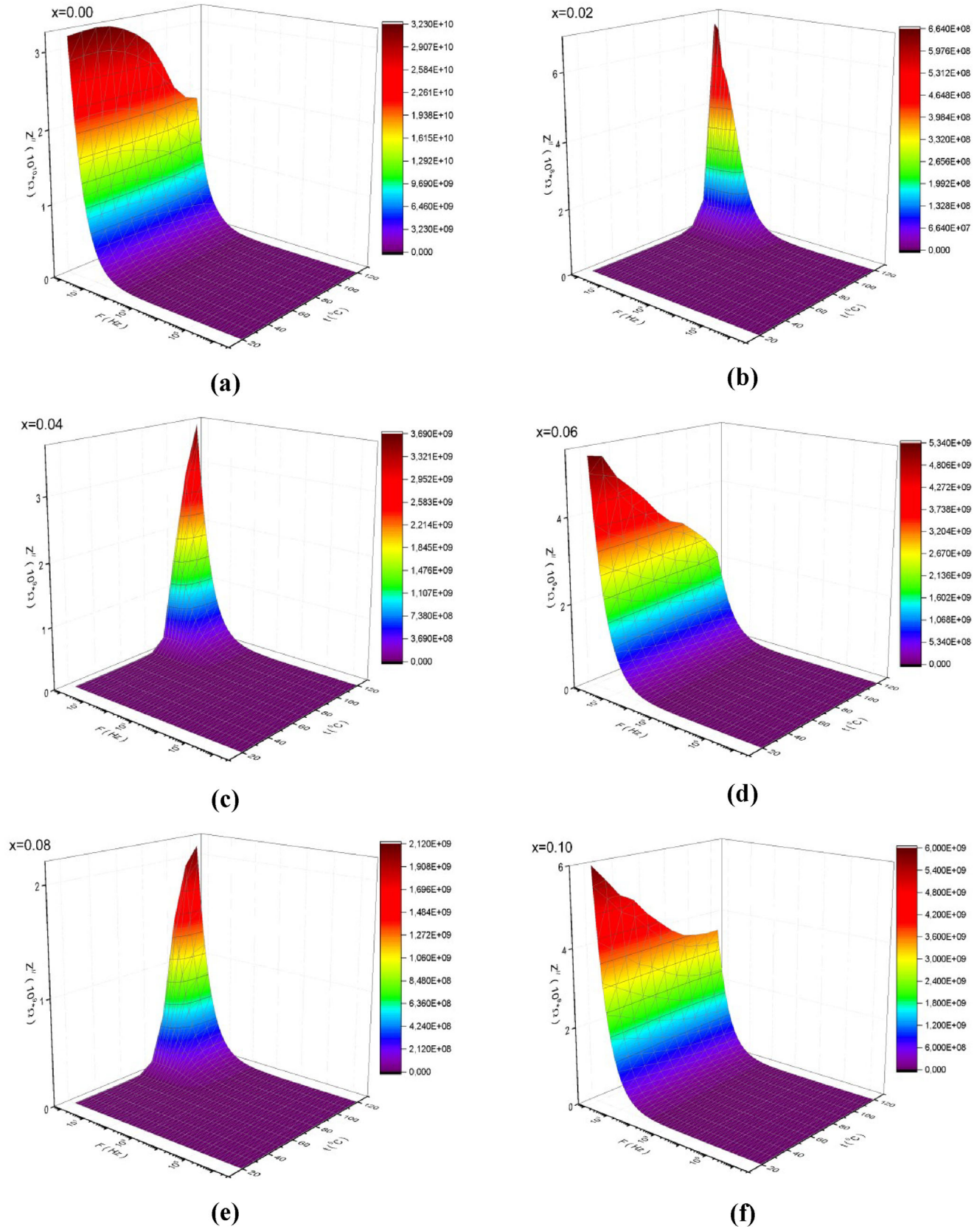

Figure 13. a–f). Frequency dependence of $Z^{//}$ impedance imaginary part of NCZ**Pd**$_x$ ($x \leq 0.1$) NSFs at different temperatures.

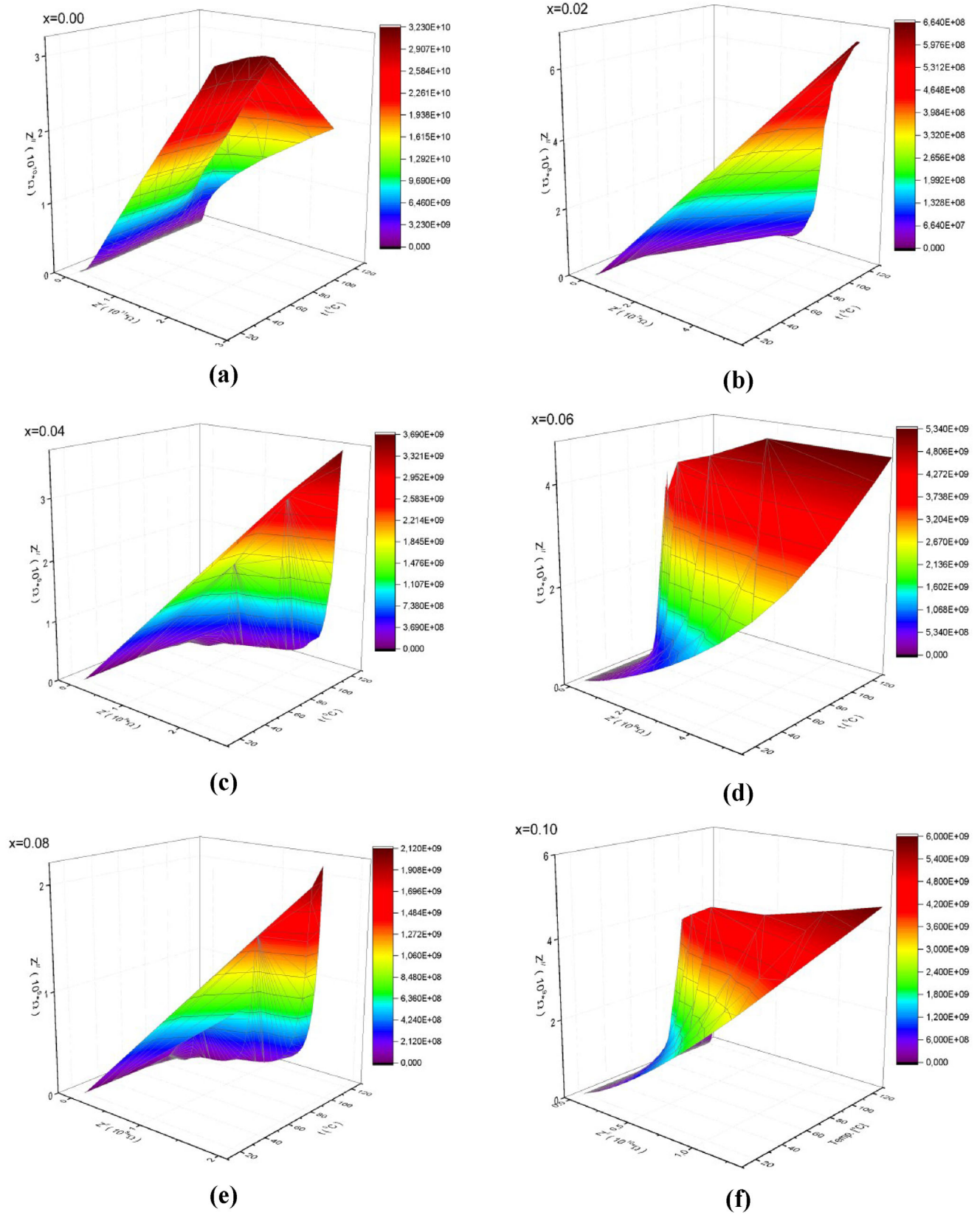

Figure 14. a–f). Experimental Nyquist diagrams $Z^{//}$ ($Z^{/}$) of NCZ**Pd**$_x$ ($x \leq 0.1$) NSFs at different temperatures.

recorded for the highly Pd-doped samples (x = 0.06–0.10), indicating stronger polarization and relaxation processes. The shift in the peak frequency of the dielectric modulus (M′) with Pd concentration and temperature confirmed the presence of thermally activated conduction mechanisms. The AC conductivity (σ) was significantly affected by Pd substitution, altering both the frequency-dependent conduction mechanism and charge carrier dynamics. The conductivity analysis demonstrated a clear distinction between low-frequency and high-frequency conduction behaviors, with DC-dominated conduction at low frequencies and hopping conduction at high frequencies, following Jonscher's universal power law. Pd incorporation modified the Fe^{2+}/Fe^{3+} redox balance, disrupted the local lattice structure, and introduced distortions that influenced charge carrier mobility and hopping length.

This study presents one of the first systematic impedance fitting and quantitative AC conductivity analyses for Pd-substituted Ni—Cu—Zn nanospinel ferrites, providing new insights into how noble metal doping influences charge transport, relaxation dynamics, and impedance behavior. These findings highlight the potential of Pd-substituted Ni—Cu—Zn ferrites for high-frequency dielectric applications, capacitive energy storage, and electromagnetic shielding technologies. The observed trends suggest that optimizing Pd content and processing conditions could further improve the functional properties of these materials for advanced electronic and magnetic applications.

4. Experimental Section

The precursors of $C_6H_8O_7$, $Fe(NO_3)_3{\cdot}9H_2O$ (≥ 98%), $Ni(NO_3)_2{\cdot}6H_2O$ (≥ 97%), $PdCl_2$ (≥ 99.9%), $Cu(NO_3)_2{\cdot}6H_2O$ (≥ 98%), $Zn(NO_3)_2{\cdot}4H_2O$ (≥ 98%) and NH_3 (25 %) solution were used as starting materials which were received Merck. The six samples with the chemical formula NCZ**Pd$_x$** ($x \leq 0.1$) NSFs were prepared by the sol–gel combustion route. While metal nitrates act as an oxidizing agent, organic fuel which provides a platform for redox reactions, citric acid (reducing agent). For specific synthesis, the stoichiometric amounts of metal nitrates (Ni, Cu, Zn, Fe) were thawed in 30 mL of deionized water (DI H_2O) until the clear solution was obtained (beaker A). The stoichiometric quantities of $PdCl_2$ corresponding to the "x" value were dissolved in beaker B containing 30 mL of cold **DI H_2O**. The metal solutions in beakers A and B were then combined, mixed with an aqueous citric acid solution, and stirred for 45 min. Subsequently, the ammonia solution was added in by drops to retain the pH to 7 while stirring. The solution was further heated from 80 to 150 °C to transform the solution (sol) into a gel, which was then automatically transformed into a fluffy powder at 320 °C within 30 min. The solid product was manually ground and calcined at 700 °C for 4 h.[20,21,17]

$$\begin{aligned} 2Fe(NO_3)_3 \cdot 9H_2O + 0.6Ni(NO_3)_2 \cdot 6H_2O + 3PdCl_2 \\ +0.2Cu(NO_3)_2 \cdot 6H_2O + 0.2Zn(NO_3)_2 \cdot 4H_2O \\ +3C_6H_8O_7 - \rightarrow Ni_{0.6}Cu_{0.2}Zn_{0.2}Pd_{3x}Fe_{2-2x}O_4\ (s) + 21.2H_2O\ (g) \\ +CO_2\ (g) + 8NO_2\ (g) + 3Cl_2\ (g) + 18CO_2\ (g) \end{aligned} \quad (6)$$

The structural investigation of products was characterized by an X-ray diffractometer from Rigaku D/MAX-2400. TEM, HR-TEM, and SEM, along with EDX were used for morphology and composition analyses. A Novocontrol Alpha impedance analyzer was used for conductivity and dielectric measurements.

Conflict of Interest

The authors declare no conflict of interest.

Data Availability Statement

The data that support the findings of this study are available from the corresponding author upon reasonable request.

Keywords

AC conductivity, dielectric properties, nanospinel ferrites, Pd substitution, sol–gel synthesis

Received: January 14, 2025
Revised: March 15, 2025
Published online: April 24, 2025

[1] B. V. Suresh, G. S. Rao, R. Y. Mudi, V. L. N. B. G. Tiruveedhi, *Inorg. Chem. Commun.* **2024**, *159*, 111850.
[2] B. Ünal, M. A. Almessiere, A. Baykal, Y. Slimani, M. A. Gondal, N. Kian-Pou, S. E. Shirsath, A. Manikandan, U. Baig, *Ceram. Int.* **2024**, *50*, 30670.
[3] Y. Guan, L. Yang, C. Chen, R. Wan, C. Guo, P. Wang, *iScience* **2025**, *28*, 111543.
[4] V. K. Raut, S. B. Somvanshi, E. A. Dawi, C. T. Birajdar, *Inorg. Chem. Commun.* **2024**, *168*, 112907.
[5] P. B. Kharat, S. B. Somvanshi, E. A. Dawi, A. M. Mopari, N. H. Bansod, *J. Mater. Sci.: Mater. Electron.* **2024**, *35*, 606.
[6] S. S. Phalake, S. B. Somvanshi, S. A. M. Tofail, N. D. Thorat, V. M. Khot, *Nanoscale* **2023**, *15*, 15686.
[7] V. K. Raut, S. B. Somvanshi, E. A. Dawi, C. T. Birajdar, *J. Sol-Gel Sci. Technol.* **2024**, *112*, 738.
[8] S. B. Somvanshi, S. A. Jadhav, S. S. Gawali, K. Zakde, K. M. Jadhav, *J. Alloys Compd.* **2023**, *947*, 169574.
[9] M. A. Almessiere, B. Ünal, Y. Slimani, A. D. Korkmaz, A. Baykal, *Results Phys.* **2019**, *15*, 102755.
[10] B. Ünal, M. A. Almessiere, A. Baykal, Y. Slimani, A. Sadaqat, A. Ul-Hamid, *Mater. Sci. Eng. B* **2023**, *289*, 116249.
[11] M. A. Munir, M. Y. Naz, S. Shukrullah, M. U. Farooq, K. Kamran, M. Irfan, A. A. J. Ghanim, *Mater. Sci. Eng. B* **2023**, *291*, 116374.
[12] Z. Cheng, X. Wang, X. Huo, Y. Jing, H. Su, *J. Magn. Magn. Mater.* **2024**, *603*, 172256.
[13] A. Baykal, Y. Slimani, M. A. Almessiere, A. D. Korkmaz, H. Güngünes, S. Caliskan, E. Arslan, S. E. Shirsath, *J. Mol. Struct.* **2025**, *1319*, 139487.
[14] Y. Yang, J. Li, C. Gan, W. Zhou, F. Xu, W. Ling, C. Chen, J. Y. Yang, J. Zhou, G. Wang, H. Zhang, *Ceram. Int.* **2024**, *50*, 7247.
[15] A. D. Korkmaz, *Mater. Sci. Eng. B* **2023**, *295*, 116598.
[16] P. K. Roy, J. Bera, *J. Magn. Magn. Mater.* **2006**, *298*, 38.
[17] M. A. Almessiere, A. Baykal, Y. Slimani, H. Güngüneş, A. Demir Korkmaz, D. S. Klygach, S. V. Trukhanov, T. I. Zubar, A. V. Trukhanov, *Appl. Phys. A* **2024**, *130*, 932.
[18] P. Vlazan, M. Poienar, F. S. Rus, P. Sfirloaga, *Phys. B: Phys. Cond. Matt.* **2021**, *615*, 413073.
[19] C. Xu, W. Sun, L. Cao, J. Yang, *Chem. Eng. J.* **2016**, *289*, 231.
[20] S. Torkian, A. Ghasemi, R. S. Razavi, *J. Magn. Magn. Mater.* **2016**, *416*, 408.
[21] M. A. Almessiere, S. Caliskan, A. Baykal, D. S. Klygach, S. V. Trukhanov, Y. Slimani, T. I. Zubar, D. A. Vinnik, A. V. Trukhanov, E. Arslan, *Mater. Sci. Eng. B* **2024**, *308*, 117571.

[22] A. D. Patil, S. M. Patange, P. M. Dighe, S. F. Shaikh, A. H. S. Rana, B. Pandit, S. S. Jadhav, *Ceram. Int.* **2022**, *48*, 27039.
[23] M. Satalkar, S. N. Kane, *J. Phys.: Conf. Ser.* **2016**, *755*, 012050.
[24] M. A. Nabi, M. Moin, M. S. Hasan, M. I. Arshad, A. Bibi, N. Amin, K. Mahmood, S. S. Ali, *J. Supercond. Nov. Magn.* **2021**, *34*, 1813.
[25] S. Md. Ullah, M. Tabassum, S. Hoque, M. Rashid, M. Harun-Or, *J. Mater. Sci.: Mater. Electron.* **2024**, *35*, 952.
[26] K. M. Batoo, G. Kumar, Y. Yang, Y. Al-Douri, M. Singh, R. B. Jotania, A. Imran, *J. Alloys Compd.* **2017**, *726*, 179.
[27] R. Rani, G. Kumar, K. M. Batoo, M. Singh, *Am. J. Nanomaterials* **2013**, *1*, 9.
[28] L. Aswaghosh, D. Manoharan, N. V. Jaya, *Phys. Chem. Chem. Phys.* **2016**, *18*, 5995.
[29] J. Massoudi, M. Smari, K. Nouri, E. Dhahri, K. Khirouni, S. Bertaina, L. Bessais, E. K. Hlil, *RSC Adv.* **2020**, *10*, 34556.
[30] N. Amri, J. Massoudi, K. Nouri, M. Triki, E. Dhahri, L. Bessais, *RSC Adv.* **2021**, *11*, 13256.
[31] M. E. Hajlaoui, R. Dhahri, N. Hnainia, A. Benchaabane, E. Dhahri, K. Khirouni, *RSC Adv.* **2019**, *9*, 32395.
[32] K. Silakaew, N. Chanlek, J. Manyam, P. Thongbai, *Res. Phys.* **2021**, *26*, 104410.
[33] P. B. Wijk, *Adv. Mol. Relax. Proces.* **1973**, *5*, 285.
[34] R. G. Raj, C. V. Krishnamurthy, *Measurement* **2020**, *151*, 107174.
[35] A. Hakeem, T. Alshahrani, G. Muhammad, M. H. Alhossainy, A. Laref, A. R. Khan, I. Ali, H. M. T. Farid, T. Ghrib, S. R. Ejaz, R. Y. Khosa, *J. Mater. Res. Technol.* **2021**, *11*, 158.
[36] T. Tatarchuk, *Nanomaterials* **2024**, *14*, 1640.
[37] V. Zviagin, M. Grundmann, R. Schmidt-Grund, *Phys. Status Solidi B* **2020**, *257*, 1900630.
[38] C. G. Koops, *Phys. Rev.* **1951**, *83*, 121.
[39] C. U. Lei, S. Ganjam, L. Krayzman, A. Banerjee, K. Kisslinger, S. Hwang, L. Frunzio, R. J. Schoelkopf, *Phys. Rev. Appl.* **2023**, *20*, 024045.
[40] L. Chauhan, S. Kumar, K. Sreenivas, A. K. Shukla, *Mater. Chem. Phys.* **2021**, *259*, 124135.
[41] S. Zhang, D. Lan, J. Zheng, Z. Zhao, Z. Jia, G. Wu, *Cell Reps. Phys. Sci.* **2024**, *5*, 102206.
[42] A. J. Williams, J. P. Attfield, S. A. T. Redfern, *Phys. Rev. B* **2005**, *72*, 184426.
[43] M. Satalkar, S. N. Kane, M. Kumaresavanji, J. P. Araujo, *Mater. Res. Bull.* **2017**, *91*, 14.
[44] E. Lim, T. Manaka, R. Tamura, M. Iwamoto, *Jpn. J. Appl. Phys.* **2006**, *45*, 3712.
[45] N. Singh, A. Agarwal, S. Sanghi, *Curr. Appl. Phys.* **2011**, *11*, 783.
[46] R. Richert, H. Wagner, *Sol. State Ion.* **1998**, *105*, 167.
[47] J. H. Ambrus, C. T. Moynihan, P. B. Macedo, *J. Phys. Chem.* **1972**, *76*, 3287.
[48] Z. Xing, C. Yin, Z. Yu, J. Khaliq, C. Li, *Ceram. Int.* **2020**, *46*, 22460.
[49] K. P. Padmasree, A. F. Fuentes, *Mater. Chem. Phys.* **2019**, *223*, 466.
[50] M. A. S. Silva, R. G. M. Oliveira, A. S. B. Sombra, *Ceram. Int.* **2019**, *45*, 20446.
[51] M. R. Eraky, S. M. Attia, *Phys. B: Condens. Matt.* **2015**, *462*, 97.
[52] R. M. Hill, *Phys. Stat. Sol. (a)* **1976**, *34*, 601.
[53] N. F. Mott, *Phil. Mag.* **1969**, *19*, 835.
[54] A. L. Efros, B. I. Shklovskii, *J. Phys. C: Solid State Phys.* **1975**, *8*, L49.
[55] Z. Li, L. Peng, J. Zhang, J. Li, Y. Zeng, Y. Luo, Z. Zhan, L. Meng, M. Zhou, W. Wu, *Semicond. Sci. Technol.* **2017**, *32*, 035010.
[56] A. Mahmood, A. Maqsood, *Mater. Sci. Eng. B* **2023**, *296*, 116615.
[57] M. Rekaby, *Appl. Phys. A* **2020**, *126*, 664.